Chemical Science

ROYAL SOCIETY OF CHEMISTRY

EDGE ARTICLE

View Article Online
View Journal | View Issue

Cite this: *Chem. Sci.*, 2024, **15**, 17103

All publication charges for this article have been paid for by the Royal Society of Chemistry

Received 26th July 2024
Accepted 23rd September 2024

DOI: 10.1039/d4sc04998e

rsc.li/chemical-science

An alternating copolymer of phenothiazine and ethylenedioxythiophene for perovskite solar cells: effects of flexible and rigid substituent alternation†

Bing Zhang, ‡ Yaohang Cai,‡ Lifei He,‡ Niansheng Xu,* Yi Yuan, Jing Zhang, Yuyan Zhang* and Peng Wang *

Developing p-type polymeric semiconductors with exceptional electrical performance, heat tolerance, and cost-effectiveness is pivotal for advancing the practical application of n-i-p perovskite solar cells. Here, we employed direct arylation polycondensation to synthesize an alternating copolymer of phenothiazine and 3,4-ethylenedioxythiophene, featuring a high glass transition temperature (175 °C). In addition to the alternation of conjugated units within the main chain, the copolymer features alternating flexible (2-octyldodecyl) and rigid (trimethylphenyl) substituents at the nitrogen positions of the phenothiazine moiety. Compared to reference polymers with solely flexible or rigid substituents, the alternating use of these moieties resulted in the polymeric semiconductor composite film with smoother morphology and enhanced hole mobility. By employing this polymer with a distinct distribution of substituents and an innovative main chain structure as a hole transport material, we fabricated perovskite solar cells achieving an average efficiency of 25.1%. These cells also exhibited excellent stabilities under conditions of 85 °C thermal storage and 45 °C operation.

1. Introduction

For high-efficiency n-i-p perovskite solar cells (PSCs) (Fig. 1A), the electron transport layer is typically fabricated from a low-cost tin dioxide colloidal solution, while the hole transport layer (HTL) commonly utilizes the molecular semiconductor spiro-OMeTAD (Fig. 1B).[1–3] spiro-OMeTAD possesses a relatively shallow highest occupied molecular orbital (HOMO) energy level, facilitating facile doping *via* fluoroalkyl sulfonyl imide salt-assisted air oxidation to achieve the moderate conductivity necessary for efficient devices. Maintaining the optimal hole density in the device, typically around 10^{18} cm^{-3}, is crucial to minimize rapid charge recombination at the perovskite/HTL interface.[4] However, the HTL composed of spiro-OMeTAD and fluoroalkyl sulfonyl imide salt typically exhibits a glass transition temperature below 85 °C. Extended exposure to high temperatures can degrade the HTL morphology, significantly reducing device efficiency.[5–7] Additionally, the conduction band offset between tin dioxide and formamidinium lead triiodide ($FAPbI_3$)-based perovskite is only a few tens of milli-electron volts. This small offset means the interfacial charge separation rate is not significantly faster than the radiative and non-radiative recombination rates in $FAPbI_3$.[8] Therefore, selecting an HTL with a sufficiently shallow HOMO energy level is crucial for achieving efficient long-range charge separation in the device. Moreover, the p-type organic semiconductor used in n-i-p PSCs must exhibit excellent film-forming property and sufficient hole conductivity, maintain its morphology under prolonged thermal stress, and effectively prevent the ingress of external species because lead halide perovskites are sensitive to moisture and tend to undergo slow decomposition *via* outgassing reactions when heated, and ions probably migrate under high electric fields.[9] To date, many polymeric semiconductors have been employed in HTLs of n-i-p PSCs, but materials that combine high performance and low cost remain scarce.[10–27]

Phenothiazine (PTZ) and ethylenedioxythiophene (EDOT) are commercially available and inexpensive fine chemicals. In single crystals, PTZ molecules adopt a non-planar butterfly conformation with a dihedral angle of 158.5° between the two benzene rings.[28] The dioxane fragment in EDOT dimers assumes a distorted chair conformation, with the sp^3 carbon atom and the thiophene ring being non-coplanar.[29] In both molecules, the lone pair electrons on nitrogen, sulfur, and oxygen atoms can engage in multi-electron p–π conjugation with π-orbital electrons. The nitrogen atom in PTZ is prone to alkylation reaction, while the para position to nitrogen on the benzene ring is susceptible to electrophilic substitution reaction. Meanwhile, the C–H bonds in the thiophene ring of EDOT can undergo highly selective activation *via* palladium catalysis.[30–39]

State Key Laboratory of Silicon and Advanced Semiconductor Materials, Department of Chemistry, Zhejiang University, Hangzhou 310058, China. E-mail: nshxu@zju.du.cn; yuyanzhang@zju.edu.cn; pw2015@zju.edu.cn

† Electronic supplementary information (ESI) available. See DOI: https://doi.org/10.1039/d4sc04998e

‡ These authors contributed equally to this work.

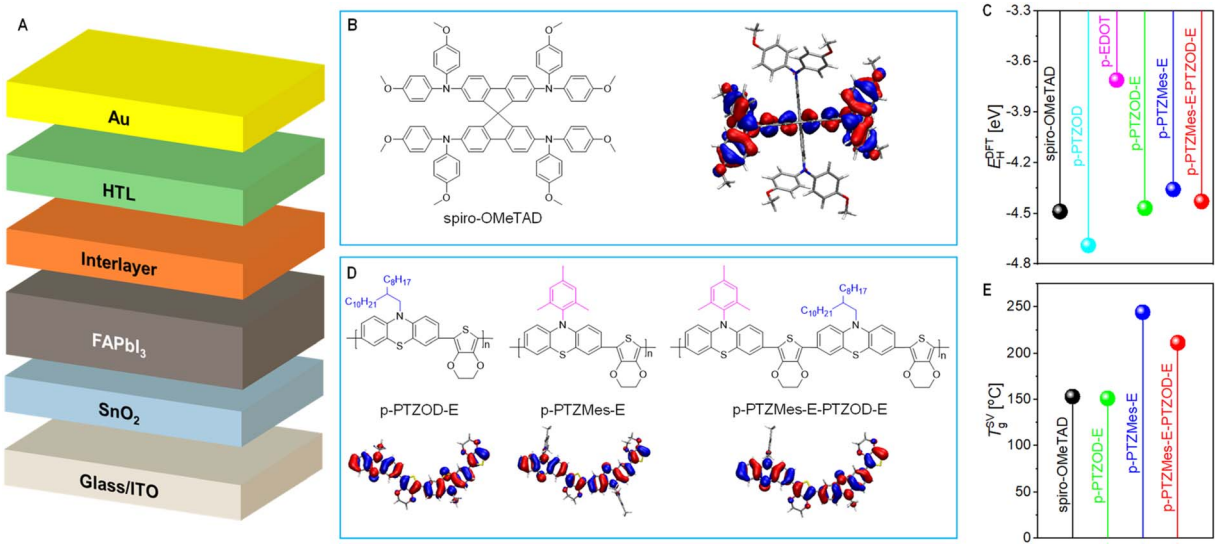

Fig. 1 (A) Schematic representation of a multilayer n-i-p perovskite solar cell. ITO denotes indium tin oxide, SnO_2 serves as the electron transport layer, $FAPbI_3$ is the light-absorbing layer, HTL stands for the hole transport layer, and Au represents the gold electrode. (B) Chemical structure of spiro-OMeTAD and contour plot of its highest occupied molecular orbital (HOMO). Isovalue: 0.02. (C) HOMO energy levels (E_H^{DFT}) obtained from density functional theory calculations. (D) Chemical structures of three phenothiazine–ethylenedioxythiophene alternating copolymers and contour plots of their HOMOs. Isovalue: 0.02. To improve computational efficiency, 2-octyldodecyl is replaced with ethyl. (E) Glass transition temperatures (T_g^{SV}) derived from molecular dynamics simulations.

In our previous study, it was found that the alternating copolymer constructed from PTZ with EDOT and aza[5]helicene showed a too deep HOMO energy level, leading to a very low efficiency of 18.4% in n-i-p PSCs.[40] Density functional theory calculations (Fig. 1C) reveal that the HOMO energy level (E_H^{DFT}) of the homopolymer of 2-octyldodecyl-substituted PTZ (p-PTZOD, structure shown in Fig. S1†) is −4.69 eV, while that of the homopolymer of EDOT (p-EDOT, Fig. S1†) is −3.71 eV. The alternating copolymer of 2-octyldodecyl-substituted PTZ and EDOT (p-PTZOD-E, Fig. 1D) exhibits an E_H^{DFT} of −4.47 eV, notably closest to that of spiro-OMeTAD (−4.49 eV) among these polymers. Molecular dynamics simulations (Fig. 1E) demonstrate that the theoretical glass transition temperature (T_g^{SV}) of p-PTZOD-E is just comparable to that of spiro-OMeTAD. Encouragingly, when 2-octyldodecyl is replaced by trimethylphenyl, the corresponding polymer (p-PTZMes-E, Fig. 1D) exhibits a T_g^{SV} as high as 244 °C. This change in substituents also significantly alters the HOMO energy level, with p-PTZMes-E having an E_H^{DFT} of −4.36 eV, which is 110 meV higher than that of p-PTZOD-E (Fig. 1C). As anticipated, when every other 2-octyldodecyl group in p-PTZOD-E is replaced with a trimethylphenyl group, the resulting polymer p-PTZMes-E-PTZOD-E (Fig. 1D) shows intermediate E_H^{DFT} and T_g^{SV} values between those of p-PTZOD-E and p-PTZMes-E (Fig. 1C and E). Frontier orbital analyses reveal that the HOMOs of these three alternating copolymers of PTZ and EDOT are relatively evenly distributed along the entire conjugated main chain (Fig. 1D). In contrast, the HOMO of spiro-OMeTAD localizes on only half of the molecular backbone due to the presence of two independent conjugated systems within the spirobifluorene structure (Fig. 1B); if HOMO can delocalize on the entire conjugated skeleton, it may increase the transfer integral of intermolecular hole hopping and reduce the reorganization energy, resulting in a higher hole mobility.

In this study, we synthesized the three target alternating copolymers of PTZ and EDOT *via* palladium-catalyzed direct arylation polycondensation. Experimental results underscored the significant influence of substituents on the molecular weight of resulting polymers under identical preparation conditions. Furthermore, the HOMO energy level of the organic semiconductor closely correlates with the rate constant for hole extraction from the excited state of $FAPbI_3$ and the hole density generated by air oxidation doping. Notably, both the HOMO energy level and the film morphology of the organic semiconductor significantly affect the efficiency of PSCs. Moreover, different HTLs exhibited marked differences in the 85 °C thermal storage stability of the devices. By utilizing the polymer p-PTZMes-E-PTZOD-E, featuring alternating flexible and rigid substituents, we fabricated PSCs achieving an average efficiency of 25.1%. This performance exceeds that of cells prepared using p-PTZOD-E (19.4%), p-PTZMes-E (23.0%), or spiro-OMeTAD (24.1%) under the same conditions. Importantly, cells based on p-PTZMes-E-PTZOD-E demonstrated excellent stabilities under thermal storage at 85 °C and operation at 45 °C.

2. Results and discussion

2.1. Synthesis and glass transition of alternating copolymers

For the synthesis, purification, and characterization of three alternating copolymers based on PTZ and EDOT, see Section 1.3 of the ESI.† Briefly, 3,7-dibromo-10-mesityl-10*H*-phenothiazine[41] and 3,7-bis(2,3-dihydrothieno[3,4-*b*][1,4]dioxin-5-yl)-10-(2-octyldodecyl)-10*H*-phenothiazine[40] were polycondensed in toluene using the catalytic system developed by Wakioka *et al.*[42]

to afford the copolymer p-PTZMes-E-PTZOD-E, featuring alternating flexible and rigid substituents. Under identical conditions, polycondensation of 3,7-dibromo-10-(2-octyldodecyl)-10*H*-phenothiazine[43] (or 3,7-dibromo-10-mesityl-10*H*-phenothiazine[41]) with EDOT yielded p-PTZOD-E (or p-PTZMes-E), with only flexible (or rigid) substituent.

High-temperature gel permeation chromatography indicated number-average molecular weights of 141 kDa (p-PTZOD-E), 4.9 kDa (p-PTZMes-E), and 152 kDa (p-PTZMes-E-PTZOD-E), relative to polystyrene standards, with polydispersity indices of 2.1, 1.9, and 1.8, respectively. Due to strong interchain interaction, poorly soluble p-PTZMes-E precipitated at a lower degree of polymerization, limiting molecular weight. Intriguingly, p-PTZMes-E-PTZOD-E, with alternating substituents, exhibited a molecular weight and a polydispersity index comparable to p-PTZOD-E.

Glass transition temperature serves as a key metric for evaluating the mechanical properties and operational temperature range of amorphous organic materials. When a material undergoes glass transition, its physical properties, particularly its tensile strength, change significantly. Differential scanning calorimetry revealed glass transition temperature (T_g^{DSC}) values of 119 °C (p-PTZOD-E), 200 °C (p-PTZMes-E), and 175 °C (p-PTZMes-E-PTZOD-E) (Fig. S2†). It is well-known that the thermal expansion coefficient of polymers exhibits a smooth step-like change during heating or cooling through the glass transition temperature. Therefore, we performed molecular dynamics simulations of a polymer with each chain having a molecular weight of approximately 10 kDa to calculate specific volumes at various temperatures. Linear fitting of specific volume data in both low- and high-temperature regions allowed us to determine the theoretical glass transition temperature (T_g^{SV}), resulting in values of 151 °C, 244 °C, and 211 °C for p-PTZOD-E, p-PTZMes-E, and p-PTZMes-E-PTZOD-E, respectively (Fig. S3A–C†). It is important to note that due to the rapid cooling rate inherent in molecular dynamics simulations, these T_g^{SV} values tend to be higher than the T_g^{DSC} values.[44] Nevertheless, a robust linear correlation exists between T_g^{SV} and T_g^{DSC} (Fig. S3D†). Our findings highlight that while incorporating the rigid trimethylphenyl substituent can elevate the glass transition temperature compared to the bulky, flexible 2-octyldodecyl substituent, achieving high molecular weight remains challenging due to solubility constraint. Alternating between these two substituents compromises the glass transition temperature but effectively modulates the molecular weight.

2.2. Energy levels and morphological characteristics of copolymer films

In n-i-p PSCs, the HOMO energy level of a p-type organic semiconductor critically influences two key processes: hole extraction from the photoexcited perovskite and doping *via* air oxidation. Initially, a solution of polymeric semiconductor was drop-cast onto glassy carbon disk electrodes and allowed to air-dry. Cyclic voltammetry measurements in acetonitrile electrolyte (0.1 M 1-ethyl-3-methylimidazolium bis(trifluoromethanesulfonyl)imide) revealed the electrochemical HOMO energy levels (E_H^{EC}) of −5.24 eV, −5.12 eV, and −5.20 eV for p-PTZOD-E, p-PTZMes-E, and p-PTZMes-E-PTZOD-E, respectively (Fig. S4A†).

Subsequently, an aqueous solution of PEDOT:PSS and a chlorobenzene solution of organic semiconductor were sequentially spin-coated onto the ITO substrate. Atomic force microscopy imaging demonstrated that spiro-OMeTAD, p-PTZOD-E, p-PTZMes-E, and p-PTZMes-E-PTZOD-E formed highly smooth amorphous films, with root-mean-square roughness values of 0.35 nm, 0.53 nm, 0.60 nm, and 0.42 nm, respectively (Fig. S5†). Ultraviolet photoelectron spectroscopy measurements of the same samples yielded the HOMO energy levels (E_H^{UPS}) of −5.08 eV, −5.00 eV, and −5.05 eV for p-PTZOD-E, p-PTZMes-E, and p-PTZMes-E-PTZOD-E, respectively (Fig. S6A–C†). Despite discrepancies in absolute HOMO values obtained from density functional theory calculation, cyclic voltammetry, and ultraviolet photoelectron spectrometry, E_H^{EC} and E_H^{UPS} showed strong linear correlations with E_H^{DFT} (Fig. S4B and S6D†).

Next, polymeric semiconductors spin-coated onto quartz substrates were analyzed *via* UV-vis absorption spectrometry to determine their optical bandgaps (E_g^{opt}, Fig. S7†), resulting in values of 2.59 eV, 2.42 eV, and 2.49 eV for p-PTZOD-E, p-PTZMes-E, and p-PTZMes-E-PTZOD-E, respectively. Combining E_H^{UPS} and E_g^{opt}, we determined the LUMO energy levels (E_L) of these polymer films using the relation $E_L = E_H^{UPS} + E_g^{opt}$. Integrating literature values for the work functions of ITO and gold electrodes, as well as the band edges of tin oxide and $FAPbI_3$,[27] we constructed an energy diagram for n-i-p PSCs, as depicted in Fig. 2A.

2.3. Hole extraction by copolymers from photoexcited perovskite

As shown in Fig. 2B, upon absorbing photons with energy higher than E_g^{opt}, electrons in the $FAPbI_3$ film are excited from the valence band to the conduction band, simultaneously generating holes in the valence band. Following ultrafast thermal relaxation, these charge carriers undergo either radiative or non-radiative recombination. Concurrently, holes that diffuse to the surface of the $FAPbI_3$ film can be extracted by the HTL. The energy difference (ΔG_{he}) between the valence band edge of the perovskite and the HOMO of the HTL influences the rate constant (k_{he}) for hole extraction. Hole extraction competes with radiative and non-radiative recombination, thereby determining the hole extraction yield (ϕ_{he}). We evaluated these parameters through time-resolved photoluminescence measurements. For details on sample preparation, measurement, and data analysis, please refer to the ESI.†

Upon excitation with a 670 nm pulsed laser, the glass-supported $FAPbI_3$ film with a polystyrene coating exhibits a slow photoluminescence decay at 810 nm, with an amplitude-weighted average lifetime (τ) of 7.3 μs (Fig. S8A and Table S1†). The reciprocal of τ represents the sum of the radiative and non-radiative rate constants. When polystyrene is replaced by one of the aforementioned organic semiconductors, τ significantly

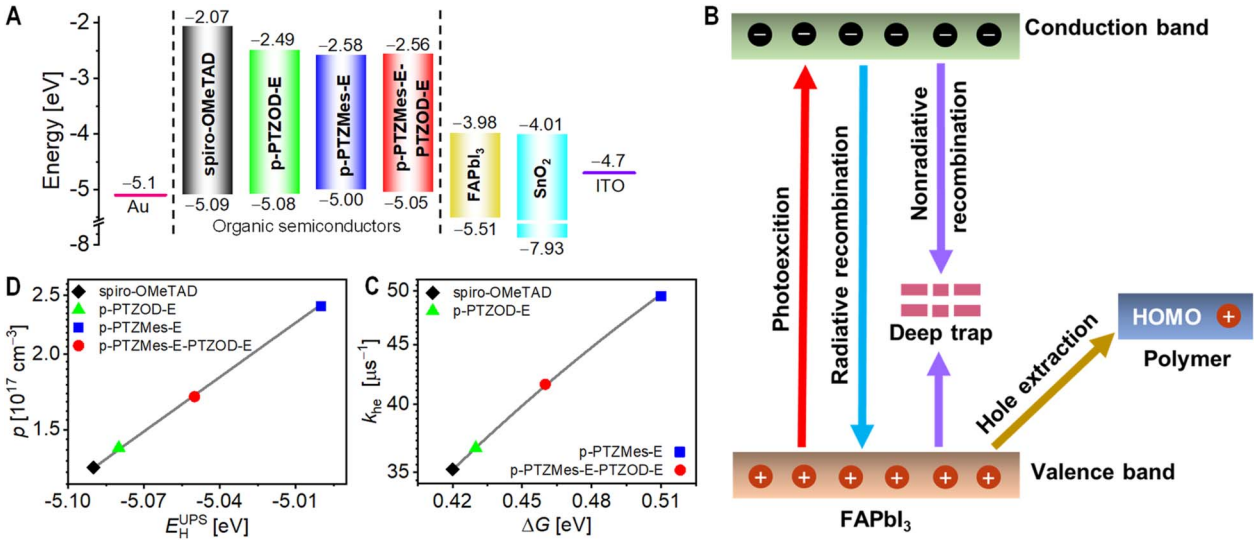

Fig. 2 (A) Energy diagram of various materials in perovskite solar cells. Numbers below and above the colored bars denote the energy levels of the valence band edge (HOMO) and conduction band edge (LUMO), respectively. Work functions of ITO and Au are also indicated. (B) Schematic depiction of photo-induced electronic processes in an $FAPbI_3$ film covered with a hole transport layer. (C) Semi-logarithmic plot showing the hole extraction rate constant (k_{he}) as a function of driving force (ΔG, the energy difference between the valence band edge of $FAPbI_3$ and the HOMO of the organic semiconductor). The grey solid line represents a nonlinear fit based on Marcus electron transfer theory. (D) Semi-logarithmic plot of hole density (p) *versus* the HOMO energy level (E_H^{UPS}) obtained from ultraviolet photoelectron spectroscopy. The grey solid line indicates a linear fit.

decreases. Specifically, the τ values for $FAPbI_3$ films coated with spiro-OMeTAD, p-PTZOD-E, p-PTZMes-E, and p-PTZMes-E-PTZOD-E are 28 ns, 27 ns, 20 ns, and 24 ns, respectively (Fig. S8B–E and Table S1†). As shown in Fig. 2C, there is a clear correlation between k_{he} and ΔG_{he} that can be described by Marcus electron transfer theory; the higher the HOMO energy level of the organic semiconductor, the larger the k_{he}. For these four organic semiconductors, the ϕ_{he} values are close to 100% (Table S1†). By comparing the spiro-OMeTAD-based samples studied in our previous work[40] and this work, it can be noted that the change of perovskite passivator from 2-phenylethylamine hydroiodide to triphenylmethane-4,4′,4″-triisocyanate can also result in the difference in k_{he}.

2.4. Hole density, conductivity, mobility, and activation energy of hole conduction in copolymer-based films

For n-i-p type PSCs, the conductivity (σ) of the HTL significantly impacts the cell's internal resistance and efficiency. σ is determined by hole density (p) and hole mobility (μ_p). Initially, we fabricated metal–insulator–semiconductor (MIS) devices and measured their impedance spectra under varying biases to derive the capacitance of the organic semiconductor layer. Using the Mott–Schottky relationship, we calculated the p values in "pristine" (as-prepared and purified; nominally undoped) organic semiconductors: spiro-OMeTAD (1.3×10^{17} cm^{-3}) < p-PTZOD-E (1.4×10^{17} cm^{-3}) < p-PTZMes-E-PTZOD-E (1.7×10^{17} cm^{-3}) < p-PTZMes-E (2.4×10^{17} cm^{-3}), as shown in Fig. 3A. For "intrinsic" (ideally pure) organic semiconductors, carriers are generated through thermally activated disproportionation reactions; for materials with an E_g^{opt} greater than 2.0 eV, the carrier density is below 10^7 cm^{-3}.[45] Clearly, holes in these "pristine" organic semiconductors must be generated through other mechanisms. The most likely mechanism is oxidative doping by atmospheric oxygen, where oxygen acts as a dopant, marginally oxidizing these high HOMO energy level organic semiconductors.[46–48] A small number of neutral organic semiconductor molecules are converted into their corresponding cation radicals, balanced electrostatically by superoxide anions generated from oxygen reduction. Interestingly, the logarithm of p shows a strong linear correlation with the E_H^{UPS} of organic semiconductor (Fig. 2D).

Clearly, the higher the HOMO energy level of an organic semiconductor, the larger the Gibbs free energy (ΔG_p) of the air oxidation doping reaction, the higher the equilibrium constant (K_p), and the higher the resulting p; the relationship between ΔG_p and K_p is described by $\Delta G_p = -RT\ln(K_p)$, where R is the gas constant and T is the temperature in Kelvin. Subsequently, we measured the σ of "pristine" organic semiconductor films using interdigital gold electrodes: p-PTZOD-E (0.01 μS cm^{-1}) < spiro-OMeTAD (0.12 μS cm^{-1}) < p-PTZMes-E-PTZOD-E (0.20 μS cm^{-1}) < p-PTZMes-E (0.23 μS cm^{-1}). Such low σ values fail to meet the PSC requirement for HTLs with low transport resistance.

To enhance the σ, we blended the fluoroalkyl sulfonyl imide salt 4-(*tert*-butyl)pyridinium 1,1,2,2,3,3-hexafluoropropane-1,3-disulfonimide (TBPH-HFSI) with the organic semiconductors.[49] This approach increases the equilibrium constant of the air oxidative doping reaction through the coupling of ion exchange and redox reactions. As shown in Fig. 3B, σ exhibits a power-law increase with the weight percentage (wt%) of TBPH-HFSI. When the wt% of TBPH-HFSI reaches 15%, the σ of the organic semiconductor composite films are: p-PTZOD-E (4.5

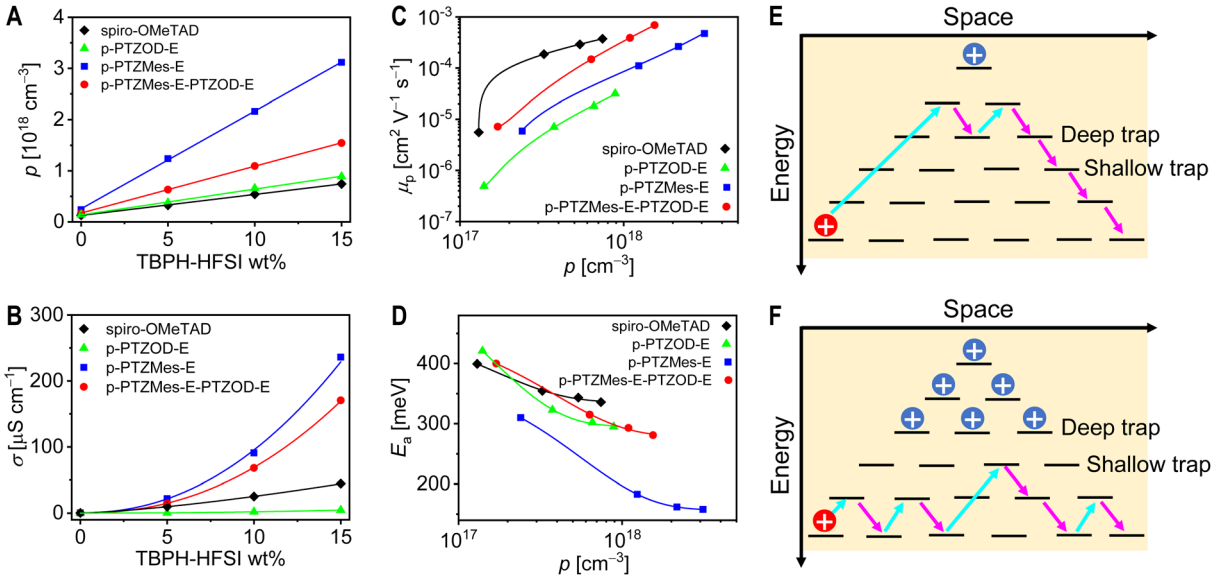

Fig. 3 (A) Relationship between hole density (p) and weight percentage (wt%) of the air oxidation doping promoter TBPH-HFSI. The solid line represents a linear fit. (B) Relationship between electrical conductivity (σ) and TBPH-HFSI wt%. The solid line indicates a power-law fit. (C) Logarithmic plot of hole mobility (μ_p) *versus* p. Solid lines serve as guides to the eye. (D) Relationship between activation energy for hole conduction (E_a) and p. The solid line represents a single-exponential decay fit. (E and F) Schematic illustration of hole transport in p-type organic semiconductors *via* thermal activation hopping. Blue spheres represent holes trapped in deep traps, while red spheres depict holes transported *via* multiple trapping (cyan) and de-trapping (magenta) processes.

μS cm^{-1}) < spiro-OMeTAD (44.4 μS cm^{-1}) < p-PTZMes-E-PTZOD-E (170.7 μS cm^{-1}) < p-PTZMes-E (236.0 μS cm^{-1}). It should be noted that accurately measuring the capacitance of TBPH-HFSI/organic semiconductor composite films using MIS devices is challenging, primarily because the contributions of the silica and polybenzocyclobutene insulating layers to the total capacitance become significant.[50] Therefore, we measured the electron paramagnetic resonance (EPR) spectra of the organic semiconductor films (Fig. S9A–D†). As shown in Fig. S9E of the ESI,† the quadratic integral of the EPR signal increases linearly with TBPH-HFSI wt%. By comparing the quadratic integrals of the EPR signals of films with and without TBPH-HFSI, and considering the p values of the "pristine" organic semiconductor films, we estimated the p values of the composite films.[8] Following the principles of chemical equilibrium, the p values of the organic semiconductor composite films indeed increase linearly with TBPH-HFSI wt%; the higher the HOMO level, the greater the increase in p (Fig. 3A), which is related to the larger equilibrium constant of the fluoroalkyl sulfonyl imide salt-assisted doping reaction.

After measuring σ and p, the μ_p was calculated using the equation $\sigma = \mu_p qp$, where q is the elementary charge. As shown in Fig. 3C, μ_p increases gradually with rising p. At the same p level, the μ_p values for the three PTZ-based alternating copolymers follow the order: p-PTZOD-E < p-PTZMes-E < p-PTZMes-E-PTZOD-E. For p-PTZOD-E, the bulky 2-octyldodecyl side chain on PTZ hinders strong π–π interactions between conjugated backbones, resulting in low μ_p. In contrast, despite having a lower molecular weight, p-PTZMes-E exhibits higher μ_p, attributable to more favorable interchain hole transport. The μ_p of p-PTZMes-E-PTZOD-E is even higher than that of p-PTZMes-E, potentially due to its higher molecular weight favoring intrachain hole transport, as well as interchain connectivity pathways. It is conceivable that in p-PTZMes-E-PTZOD-E, despite half of the PTZ units being substituted with bulky 2-octyldodecyl side chains, strong π–π interactions between PTZMes-EDOT segments may induce a preferential perpendicular local orientation between polymer chains. These interchain π-crossing points might facilitate a mesh-like structure, providing effective pathways for interchain charge transport.[51] Alternating flexible and rigid substituents demonstrated here appears to be an effective strategy for enhancing the mobility of polymeric semiconductors. We conducted GIWAXS measurements on p-PTZOD-E, p-PTZMes-E, and p-PTZMes-E-PTZOD-E thin films, all of which exhibited amorphous characteristics, complicating the evaluation of intermolecular π–π interactions. To address this, future studies could employ advanced solid-state nuclear magnetic resonance techniques, integrated with complementary experimental and computational approaches, to better establish structure–property relationships in these complex materials.[52]

It is well recognized that charge carriers in organic semiconductors exhibit a strong localized character, with the density of states typically following a Gaussian or exponential distribution, and carrier transport occurring *via* a thermally activated hopping mechanism.[53] We measured the σ of the aforementioned films at different temperatures (Fig. S10†), finding that it increases with rising temperature. Using the Arrhenius equation to analyze the temperature-dependent σ, we determined the activation energy (E_a) for hole conduction. The results show that E_a decreases exponentially with increasing p (Fig. 3D).[54,55] As illustrated in Fig. 3E, at low p, all holes are trapped in deep

traps, resulting in high hopping activation energy and low μ_p. Conversely, as depicted in Fig. 3F, at high p, deep traps are filled by some holes, leaving the remaining holes in shallow traps, which have low hopping activation energy, leading to high μ_p.

2.5. Application in PSCs

2.5.1. Photovoltaic characteristics and physical analysis. We fabricated PSCs with an ITO/SnO_2/$FAPbI_3$/TTI-derived interlayer/HTL/Au structure, using an 85/15 weight ratio blend of the organic semiconductor and the air-doping promoter TBPH-HFSI as the HTL. TTI refers to triphenylmethane triisocyanate. Detailed methods for cell fabrication and characterization are provided in the ESI,† Section 1.9. The photocurrent density–voltage (J–V) curves of the cells were measured under simulated AM1.5G sunlight at 100 mW cm^{-2}. The statistical distribution of photovoltaic parameters (short-circuit photocurrent density, J_{SC}; open-circuit voltage, V_{OC}; fill factor, FF; power conversion efficiency, PCE) for eight cells is shown in Fig. S11 of the ESI.† The reverse scan curves for representative cells are plotted in Fig. 4A, and the corresponding photovoltaic parameters are listed in Table 1. The p-PTZOD-E cell exhibited the lowest J_{SC}, V_{OC}, and FF, at 25.10 mA cm^{-2}, 1.110 V, and 69.8%, respectively, resulting in the lowest PCE (19.4%). In contrast, the p-PTZMes-E cell demonstrated higher J_{SC} (25.54 mA cm^{-2}), V_{OC} (1.165 V), and FF (77.3%), leading to a higher PCE (23.0%). The p-PTZMes-E-PTZOD-E cell showed the highest J_{SC}, V_{OC}, and FF, at 26.09 mA cm^{-2}, 1.180 V, and 81.6%, respectively, achieving a PCE of 25.1%. Additionally, the reference cell based on spiro-OMeTAD exhibited a PCE of 24.1% (J_{SC} = 26.09 mA cm^{-2}, V_{OC} = 1.185 V, FF = 78.0%). We also compared the reverse and forward scan curves, affording the hysteresis index. For the p-PTZMes-E-PTZOD-E cell, the hysteresis index was as small as 0.4% (Fig. S12†). When the bias voltage was switched from the open-circuit voltage to the maximum power point voltage, the photocurrent quickly reached a steady state; for the p-PTZMes-E-PTZOD-E cell, the steady-state PCE output was 25.0% (Fig. S13†), consistent with the J–V result.

Subsequently, we measured the external quantum efficiencies (EQEs) of the aforementioned cells under monochromatic light irradiation (Fig. 4B). Combining EQE spectra with the standard AM1.5G solar spectrum (ASTM G173-03) allowed us to predict the short-circuit photocurrent density (J_{SC}^{EQE}) under AM1.5G conditions. The results revealed a linear correlation between J_{SC}^{EQE} and J_{SC} (Fig. S14†). Furthermore, the J_{SC}^{EQE} closely matched J_{SC}, indicating minimal mismatch in the solar simulator used for J–V measurements. For the cells with p-PTZMes-E-PTZOD-E and spiro-OMeTAD, EQEs exceeded 90% in the 400–750 nm wavelength range, peaking near 95%. In contrast, cells based on p-PTZOD-E and p-PTZMes-E exhibited decreased EQEs within this range. The decline in EQE intensified with longer wavelengths in the 550–700 nm range, more pronounced in the p-PTZOD-E cell compared to p-PTZMes-E. This EQE deterioration correlates with accelerated recombination of electrons from the perovskite film with holes in the HTLs. The closer proximity of electrons in the perovskite film to the p-PTZMes-E and p-PTZOD-E based HTLs enhances recombination probability, as evidenced by the amplified EQE decay with increasing wavelength. This rapid charge recombination contributes to the observed lower V_{OC} in the J–V measurements.

Next, we measured the electroluminescence external quantum efficiencies (EQE_{EL}) of the aforementioned cells. At an injected current density of 26 mA cm^{-2}, the EQE_{EL} values for the four cells were as follows: spiro-OMeTAD (6.8%) > p-PTZMes-E-PTZOD-E (6.4%) > p-PTZMes-E (3.9%) > p-PTZOD-E (0.9%) (Fig. 4C). The non-radiative open-circuit photovoltage loss (ΔV_{OC}^{nr}) can be calculated using the formula $\Delta V_{OC}^{nr} = -\frac{k_B T}{q}\ln(EQE_{EL})$, where k_B is the Boltzmann constant, T

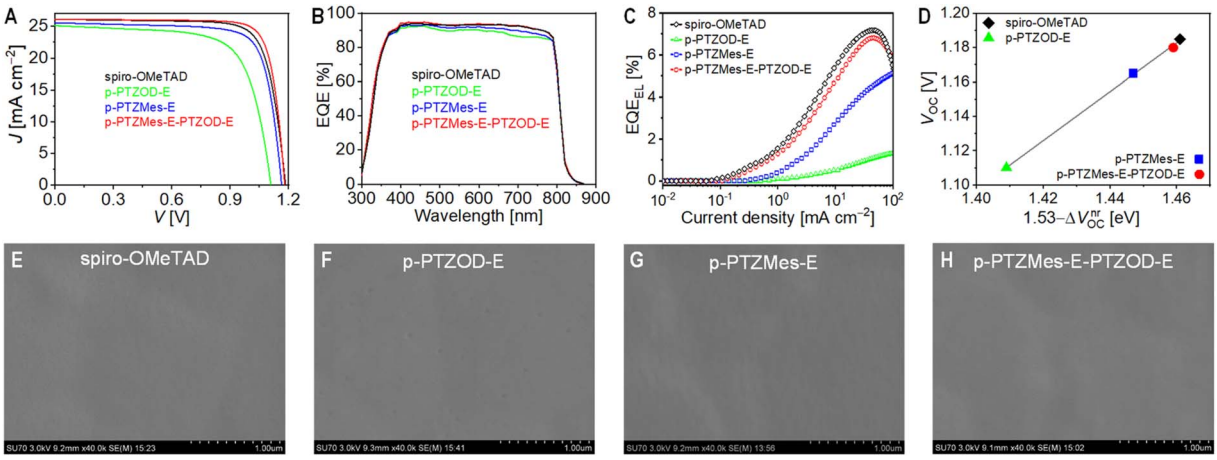

Fig. 4 (A) Representative reverse photocurrent density–voltage (J–V) curves of perovskite solar cells employing different hole transport layers under simulated AM1.5G irradiation at 100 mW cm^{-2}. (B) External quantum efficiency (EQE) spectrum. (C) Electroluminescence external quantum efficiency (EQE_{EL}) plotted as a function of current density. (D) Relationship between open-circuit voltage (V_{OC}) and non-radiative recombination V_{OC} loss (ΔV_{OC}^{nr}). The optical bandgap of the perovskite absorber layer is 1.53 eV. The grey solid line indicates a linear fit. (E–H) Scanning electron microscopy images of hole transport layers in perovskite solar cells: (E) spiro-OMeTAD; (F) p-PTZOD-E; (G) p-PTZMes-E; (H) p-PTZMes-E-PTZOD-E. Scale bar: 1 μm. Images were taken after removal of encapsulation materials and the gold electrode.

Table 1 Photovoltaic parameters and diode parameters for representative cells under the simulated AM1.5G irradiation[a]

Cell	J_{SC} [mA cm^{-2}]	V_{OC} [V]	FF [%]	PCE [%]	J_{SC}^{EQE} [mA cm^{-2}]	n	I_s [10^{-18} A]	R_s [Ω]	R_{sh} [kΩ]
Spiro-OMeTAD	26.09	1.185	78.0	24.1	25.67	1.35	3.0	31.7	26.2
p-PTZOD-E	25.10	1.110	69.8	19.4	24.64	1.25	3.0	65.9	5.3
p-PTZMes-E	25.54	1.165	77.3	23.0	25.07	1.33	3.0	15.0	10.2
p-PTZMes-E-PTZOD-E	26.09	1.180	81.6	25.1	25.65	1.35	3.0	19.4	26.2

[a] J_{SC}: short-circuit photocurrent density; V_{OC}: open-circuit voltage; FF: fill factor; PCE: power conversion efficiency; J_{SC}^{EQE}: the integral of the product of the EQE and the photo flux of the AM 1.5G emission (ASTM G173-03) over the wavelength; n: ideality factor; I_s: reverse saturation current; R_s: series resistance; R_{sh}: shunt resistance. The aperture area of metal mask: 0.07 cm^2.

is the temperature in Kelvin, and q is the elementary charge.[56] The ΔV_{OC}^{nr} values for the four cells were: spiro-OMeTAD (69 mV) < p-PTZMes-E-PTZOD-E (71 mV) < p-PTZMes-E (83 mV) < p-PTZOD-E (121 mV). By differentiating the EQE spectrum of the p-PTZMes-E-PTZOD-E cell (Fig. S15†), we estimated the optical bandgap of the $FAPbI_3$-based light absorption layer to be 1.53 eV. Moreover, V_{OC} shows a strong linear correlation with $1.53 - \Delta V_{OC}^{nr}$ (Fig. 4D). The smaller the ΔV_{OC}^{nr}, the higher the V_{OC}.

Additionally, we measured the V_{OC} of the cells under different irradiances (Fig. S16†). By plotting V_{OC} against the logarithm of the irradiance, we calculated the ideality factor (n)[57] for each cell: p-PTZOD-E (1.25) < p-PTZMes-E (1.33) < p-PTZMes-E-PTZOD-E (1.35) = spiro-OMeTAD (1.35) (Fig. S17†). The n reflects the inverse of the order of nonlinear charge recombination reactions in the cells, with n values (>1) indicating the presence of localized states in the semiconductors.[58] Using the Shockley diode equation[59] and these n values, we fitted the J–V curves to obtain the shunt resistance (R_{sh}), series resistance (R_s), and reverse saturation current (I_s) (Table 1). The results indicate that higher R_{sh} leads to higher V_{OC}, while lower R_s and higher R_{sh} result in higher FF. Compared to spiro-OMeTAD, the higher FF of the p-PTZMes-E-PTZOD-E cell is attributed to its lower R_s, which is associated with the higher HOMO level of its HTL, leading to faster hole extraction rate and higher conductivity. The lowest FF of the p-PTZOD-E cell is mainly due to its lowest R_{sh} and highest R_s, the latter being associated with the slowest hole extraction rate and lowest conductivity, stemming from the deepest HOMO energy level of its HTL. Although the HTL of the p-PTZMes-E cell exhibits the fastest hole extraction rate and highest conductivity (highest HOMO level), it shows a moderate FF, mainly due to its low R_{sh}, which might be related to an excessively high hole density. To confirm this inference, we also prepared the p-PTZMes-E cell with a reduced TBPH-HFSI wt% (10%), which showed slight improvements in J_{SC} (25.72 mA cm^{-2}), V_{OC} (1.170 V), FF (78.5%), and PCE (23.6%).

Next, we removed the encapsulation materials and gold electrode from the PSCs and performed the morphology analysis of the HTLs. Atomic force microscopy images (Fig. S18†) showed that the polycrystalline perovskite thin film had a relatively high root-mean-square roughness of 37 nm. Following the deposition of an HTL, the roughness was significantly reduced, with the values decreasing in the order: p-PTZMes-E (16 nm) > p-PTZMes-E-PTZOD-E (15 nm) > p-PTZOD-E (10 nm) = spiro-OMeTAD (10 nm). Scanning electron microscopy image revealed that on the surface of the perovskite microcrystalline film (Fig. S19†), the HTLs based on spiro-OMeTAD and p-PTZMes-E-PTZOD-E were very intact (Fig. 4E and H), while the HTL based on p-PTZMes-E showed some wrinkles (Fig. 4G). In contrast, the HTL based on p-PTZOD-E exhibited some submicron pits (Fig. 4F). Interestingly, when TBPH-HFSI in the p-PTZOD-E-based HTL was replaced with an equal wt% of 4-(*tert*-butyl)pyridinium bis(trifluoromethanesulfonyl)imide (TBPH-TFSI),[60] the film morphology deteriorated further, showing significant phase separation between TBPH-TFSI and the polymeric semiconductor (Fig. S20A†). Note that TBPH-TFSI and TBPH-HFSI are two different organic salts, with the difference being the chemical structures of the anions. Notably, the "pristine" p-PTZOD-E film exhibited a complete morphology (Fig. S20B†). These comparative experiments suggest that the morphology of the composite film is likely controlled by the miscibility of the organic salt (doping promoter) with the polymeric semiconductor. An incomplete HTL morphology may lead to microscopic contacts between the gold electrode and the perovskite, introducing new charge recombination pathways and resulting in low R_{sh}.

The above analyses indicated that when designing hole transport materials for n-i-p PSCs, it is necessary to consider the combined quality factors including HOMO energy level, film-forming property, and hole mobility. These physical attributes, as well as doping (hole density and conductivity) control of organic semiconductors, will affect the charge separation and charge recombination of PSCs, ultimately affecting various photovoltaic parameters of the device.

2.5.2. Storage stability at 85 °C and degradation analysis. To assess thermal storage stability, we placed the cells in the oven at 85 °C (ISOS-D-2) and periodically measured their J–V curves under AM1.5G solar illumination at room temperature. As shown in Fig. 5A, after 1000 hours, the PCE retention rates for the representative cells with p-PTZMes-E and p-PTZMes-E-PTZOD-E were 89% and 90%, respectively, significantly higher than those of the cells with spiro-OMeTAD (72%) and p-PTZOD-E (35%). Fig. 5B presents the J–V curves after 1000 hours of aging, with the corresponding photovoltaic parameters detailed in Table S2 of the ESI.† Comparing the photovoltaic parameters in Tables 1 and S2 of the ESI,† we observed that thermal aging resulted in an 11.5% reduction in J_{SC}, a 6.3% reduction in V_{OC}, and a 13.2% reduction in FF for the spiro-OMeTAD cell, while the p-PTZOD-E cell exhibited reductions of 22.1%, 18.0%, and 46.8% in J_{SC}, V_{OC}, and FF, respectively. In contrast, the J_{SC}, V_{OC},

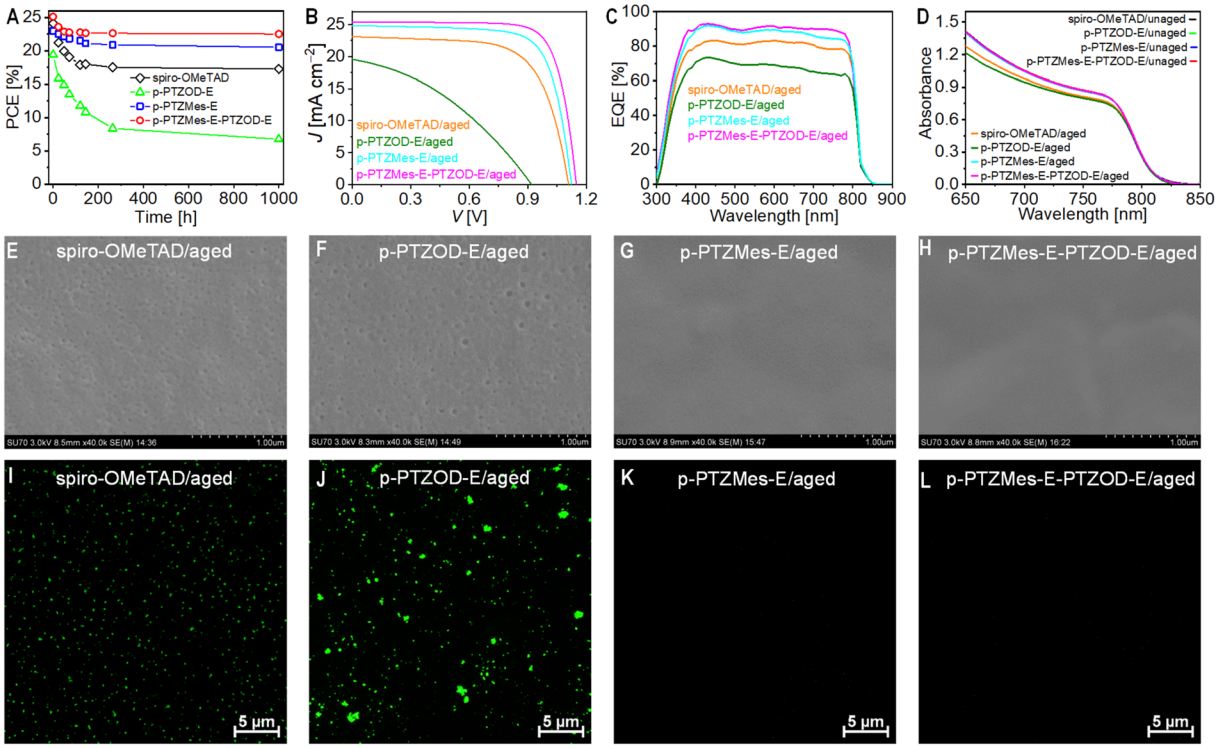

Fig. 5 (A) Power conversion efficiency (PCE) *versus* time of aging at 85 °C (ISOS-D-2) for solar cells with different hole transport layers. (B) Reverse scan photocurrent density–voltage (*J*–*V*) curves of aged cells under 100 mW cm^{-2} simulated AM1.5G irradiation. (C) External quantum efficiency (EQE) spectra of aged cells. (D) Electronic absorption spectra of cells before and after aging. No clear difference can be observed for the unaged cells, the aged p-PTZMes-E cell, and the aged p-PTZMes-E-PTZOD-E cell. (E–H) Top-view scanning electron microscopy images of the hole transport layers in aged cells: (E) spiro-OMeTAD; (F) p-PTZOD-E; (G) p-PTZMes-E; (H) p-PTZMes-E-PTZOD-E. Scale bar: 1 μm. (I–L) Fluorescence optical microscopy images of the perovskite layers in aged cells: (I) spiro-OMeTAD; (J) p-PTZOD-E; (K) p-PTZMes-E; (L) p-PTZMes-E-PTZOD-E. Scale bar: 5 μm. For panels (D–H), encapsulation material and gold electrode were removed before measurement. For panels (I–L), encapsulation material, gold electrode, and hole transport layer were removed before measurement. Aging conditions: 85 °C for 1000 hours.

and FF reductions for the p-PTZMes-E cell were 2.8%, 3.4%, and 5.2%, respectively; for the p-PTZMes-E-PTZOD-E cell, these parameters decreased by only 2.7%, 2.5%, and 5.6%, respectively. As shown in Fig. 4B and 5C, after 1000 hours of thermal aging, the maximum EQE of the p-PTZOD-E cell decreased from 92% to 73%, while for the spiro-OMeTAD cell, it decreased from 94% to 83%. In contrast, the maximum EQE values of the cells with p-PTZMes-E and p-PTZMes-E-PTZOD-E decreased by less than 2%. As shown in Fig. S21 of the ESI,† there was a good linear correlation between J_{SC} and J_{SC}^{EQE} regardless of whether the cells were aged or not.

Next, we removed the encapsulation materials and gold electrode from the PSCs and measured their UV-vis absorption spectra (Fig. 5D). The results revealed that thermal aging significantly diminished the light absorption of the spiro-OMeTAD and p-PTZOD-E cells, potentially due to perovskite decomposition or phase transformation. In contrast, the light absorption of the p-PTZMes-E and p-PTZMes-E-PTZOD-E cells remained nearly unchanged. Time-resolved photoluminescence measurements (Fig. S22†) showed an increase in τ due to thermal aging, with the extent of increase as follows: p-PTZOD-E (320%) > spiro-OMeTAD (230%) > p-PTZMes-E (120%) > p-PTZMes-E-PTZOD-E (50%). We noticed that the difference in hole extraction rate by a doped organic semiconductor (Section 2.3) and the corresponding "pristine" organic semiconductor in PSC is not significant, because introducing air-doping promoter only increased the hole density from the order of 10^{17} cm^{-3} to the order of 10^{18} cm^{-3}. A further study could be performed on the impact of low concentration doping on the distribution of gap states in these organic semiconductors.[61,62] The elevated τ in aged cells may correlate with the formation of wide bandgap species at the perovskite/HTL interface.

Scanning electron microscope images revealed numerous nanopores in the HTLs of aged spiro-OMeTAD and p-PTZOD-E cells (Fig. 5E and F), with larger pores observed in the p-PTZOD-E cell. It is noted that the glass transition temperatures of "pristine" p-PTZOD-E (119 °C) and spiro-OMeTAD (121 °C) are comparable. However, PSCs based on p-PTZOD-E exhibit poorer stability and more pronounced morphological degradation in the hole transport layer, likely due to the already presence of pits in the unaged p-PTZOD-E-based cells. This suggests that both the glass transition temperature and the morphology of the hole transport materials play critical roles in determining the thermal stability of PSCs at 85 °C. It is also worth noting that blending organic salts with organic semiconductors tends to lower the glass transition temperature.[7] In stark contrast, the

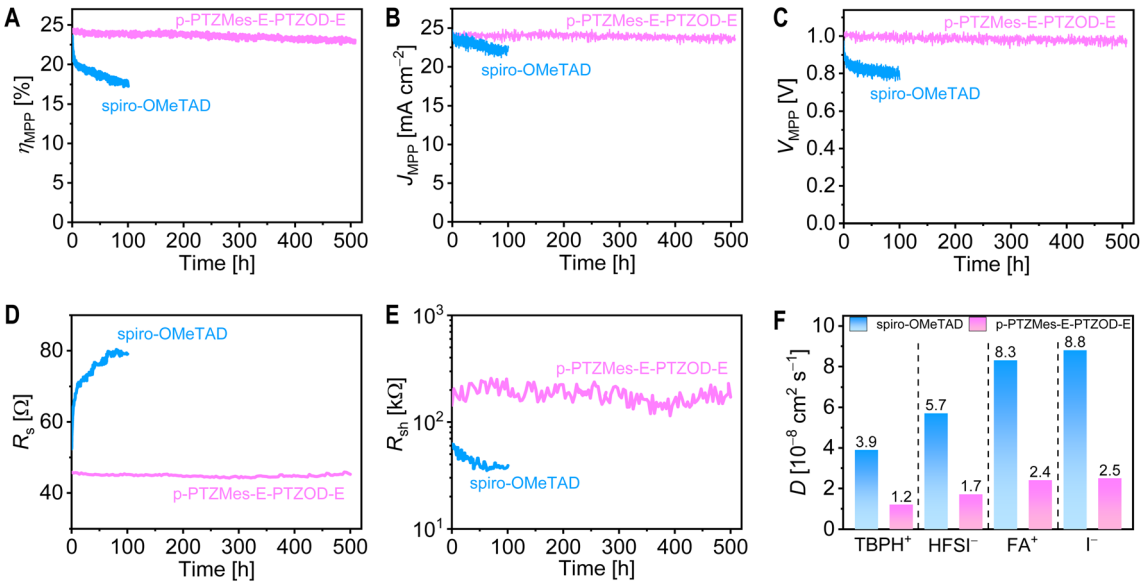

Fig. 6 (A–C) Photovoltaic parameters tracked at the maximum power point (MPP) under simulated AM1.5G irradiation at 100 mW cm^{-2}: (A) efficiency at MPP (η_{MPP}); (B) photocurrent density at MPP (J_{MPP}); (C) photovoltage at MPP (V_{MPP}). (D and E) Series resistance (R_s) and shunt resistance (R_{sh}) obtained from fitting the J–V curves measured intermittently during MPP tracking. (F) Ion diffusion coefficients (D) in the hole transport layer at 45 °C.

HTLs of the p-PTZMes-E-PTZOD-E and p-PTZMes-E cells maintained their integrity (Fig. 5G and H). Severe degradation of the HTL morphology may result in contacts between the gold electrode and the perovskite, thereby decreasing V_{OC}.

Furthermore, fluorescence microscopy imaging of the perovskite layer after chlorobenzene washing of the HTL showed no discernible patterns in unaged cells (Fig. S23†). After aging, the perovskite layers of spiro-OMeTAD and p-PTZOD-E cells exhibited dense green spots (Fig. 5I and J), likely due to G-band luminescence from PbI_2. In contrast, the perovskite layers of p-PTZMes-E and p-PTZMes-E-PTZOD-E cells showed only a few smaller green spots (Fig. 5K and L). Perovskite degradation could diminish light harvesting and induce more structural defects, including deep trap states that reduce charge separation and collection efficiencies, thereby degrading the device's photovoltaic parameters.

2.5.3. Operational stability. Subsequently, under a nitrogen atmosphere, we employed the perturbation and observation method to conduct maximum power point tracking (MPPT) on the high-efficiency spiro-OMeTAD and p-PTZMes-E-PTZOD-E cells. Fig. 6A–C illustrate the temporal evolution of conversion efficiency (η_{MPP}), photocurrent density (J_{MPP}), and photovoltage (V_{MPP}) at the maximum power point under simulated AM1.5G solar illumination at 45 °C. After 100 hours, the η_{MPP} of the spiro-OMeTAD cell decreased to 17.3% (initially 23.6%), primarily due to an 8.5% reduction in J_{MPP} and a 20.3% reduction in V_{MPP}. In contrast, after 500 hours, the η_{MPP} of the p-PTZMes-E-PTZOD-E cell decreased only slightly from 24.4% to 23.1%, demonstrating an efficiency retention rate of 95%.

During MPPT, we intermittently measured the J–V curves of the cells and fitted them using the Shockley diode equation[59] to extract R_s and R_{sh}. The time-dependent changes in R_s and R_{sh} are shown in Fig. 6D and E. Over time, R_s for the spiro-OMeTAD cell exhibited a gradual increase, while R_{sh} decreased. In contrast, the variations in R_s and R_{sh} for the p-PTZMes-E-PTZOD-E cell were less pronounced. The reduction in R_{sh} indicates accelerated charge recombination, likely associated with increased perovskite defects. The increase in R_s may arise from enhanced defects and scattering centers within the perovskite, or possibly from iodide ion migration from the perovskite to the HTL under an electric field, leading to dedoping.[63] Molecular dynamics simulations were performed to investigate the diffusion behavior of relevant ions (4-(*tert*-butyl)pyridinium, TBPH$^+$; 1,1,2,2,3,3-hexafluoropropane-1,3-disulfonimide, HFSI$^-$; formamidinium, FA$^+$; iodide, I$^-$) in both HTLs. These simulations revealed smaller diffusion coefficients for these ions in the p-PTZMes-E-PTZOD-E-based HTL compared to spiro-OMeTAD (Fig. 6F). Suppressing species diffusion within PSCs could effectively regulate defect formation in the perovskite layer and dedoping processes.

3. Conclusions

Through direct arylation polymerization, we synthesized three phenothiazine–ethylenedioxythiophene alternating copolymers featuring varied substituents on phenothiazine: one with 2-octyldodecyl, another with trimethylphenyl, and a third alternating between 2-octyldodecyl and trimethylphenyl groups. This substitution variation led to differences in the HOMO energy levels of the polymeric semiconductors, influencing air oxidation doping and the rate of hole extraction from photoexcited perovskite. These phenothiazine–ethylenedioxythiophene copolymers demonstrated hole density-dependent mobility and conductivity. The combined use of flexible and rigid substituents endowed the polymeric semiconductor composite film with a more uniform

surface morphology and enhanced hole mobility. These attributes bolster the efficiency and stability of perovskite solar cells. This work presents a novel strategy for crafting high-performance polymeric semiconductors. While we did not prepare the random copolymers of phenothiazine and ethylenedioxythiophene with flexible 2-octyldodecyl and rigid trimethylphenyl side chains in the present work. It will be interesting to optimize the side chain ratios in the random copolymers.

Data availability

All the data supporting this article have been included in the main text and the ESI.†

Author contributions

Conceptualization: P. W. Data curation: B. Z.; Y. C.; L. H. Funding acquisition: Y. Y.; P. W. Investigation: B. Z.; Y. C.; L. H.; N. X.; Y. Y.; J. Z.; Y. Z. Methodology: Y. Z. Project administration: Y. Y. Supervision: N. X. Validation: N. X; J. Z. Visualization: Y. C.; Y. Z. Writing – original draft: Y. C.; Y. Z. Writing – review & editing: N. X.; P. W.

Conflicts of interest

There are no conflicts to declare.

Acknowledgements

The authors thank the National Key Research and Development Program of China (2022YFA1204800) and the National Natural Science Foundation of China (No. 22275160, No. 22475187, and No. 52073250) for the financial support. The authors thank Yifan Zhao from the Chemistry Instrumentation Center Zhejiang University for the technical support.

References

1 M. Kim, J. Jeong, H. Lu, T. K. Lee, F. T. Eickemeyer, Y. Liu, I. W. Choi, S. J. Choi, Y. Jo, H.-B. Kim, S.-I. Mo, Y.-K. Kim, H. Lee, N. G. An, S. Cho, W. R. Tress, S. M. Zakeeruddin, A. Hagfeldt, J. Y. Kim, M. Grätzel and D. S. Kim, *Science*, 2022, **375**, 302.
2 Y. Zhao, F. Ma, Z. Qu, S. Yu, T. Shen, H.-X. Deng, X. Chu, X. Peng, Y. Yuan, X. Zhang and J. You, *Science*, 2022, **377**, 531.
3 J. Park, J. Kim, H.-S. Yun, M. J. Paik, E. Noh, H. J. Mun, M. G. Kim, T. J. Shin and S. I. Seok, *Nature*, 2023, **616**, 724.
4 L. He, Y. Zhang, Y. Wei, Y. Cai, J. Zhang and P. Wang, *Matter*, 2023, **6**, 4013.
5 X. Zhao, H.-S. Kim, J.-Y. Seo and N.-G. Park, *ACS Appl. Mater. Interfaces*, 2017, **9**, 7148.
6 A. K. Jena, M. Ikegami and T. Miyasaka, *ACS Energy Lett.*, 2017, **2**, 1760.
7 Y. Wei, Y. Zhang, Y. Ren, B. Zhang, Y. Yuan, J. Zhang and P. Wang, *Adv. Funct. Mater.*, 2023, **33**, 2307501.
8 Y. Ren, Y. Wei, T. Li, Y. Mu, M. Zhang, Y. Yuan, J. Zhang and P. Wang, *Energy Environ. Sci.*, 2023, **16**, 3534.
9 C. C. Boyd, R. Cheacharoen, T. Leijtens and M. D. McGehee, *Chem. Rev.*, 2019, **119**, 3418.
10 Z. Zhu, Y. Bai, H. K. H. Lee, C. Mu, T. Zhang, L. Zhang, J. Wang, H. Yan, S. K. So and S. Yang, *Adv. Funct. Mater.*, 2014, **24**, 7357.
11 S. Ryu, J. H. Noh, N. J. Jeon, Y. C. Kim, W. S. Yang, J. Seo and S. I. Seok, *Energy Environ. Sci.*, 2014, **7**, 2614.
12 J. Lee, M. M. Byranvand, G. Kang, S. Y. Son, S. Song, G.-W. Kim and T. Park, *J. Am. Chem. Soc.*, 2017, **139**, 12175.
13 L. Zhang, C. Liu, J. Zhang, X. Li, C. Cheng, Y. Tian, A. K.-Y. Jen and B. Xu, *Adv. Mater.*, 2018, **30**, 1804028.
14 Y. Kim, E. H. Jung, G. Kim, D. Kim, B. J. Kim and J. Seo, *Adv. Energy Mater.*, 2018, **8**, 1801668.
15 L. Zhang, C. Liu, X. Wang, Y. Tian, A. K. Y. Jen and B. Xu, *Adv. Funct. Mater.*, 2019, **29**, 1904856.
16 J. Lee, G.-W. Kim, M. Kim, S. A. Park and T. Park, *Adv. Energy Mater.*, 2020, **10**, 1902662.
17 G. You, Q. Zhuang, L. Wang, X. Lin, D. Zou, Z. Lin, H. Zhen, W. Zhuang and Q. Ling, *Adv. Energy Mater.*, 2020, **10**, 1903146.
18 J. Park, S. E. Yoon, J. Lee, D. R. Whang, S. Y. Lee, S. J. Shin, J. M. Han, H. Seo, H. J. Park, J. H. Kim and B.-G. Kim, *Adv. Funct. Mater.*, 2020, **30**, 2001560.
19 Q. Fu, Z. Xu, X. Tang, T. Liu, X. Dong, X. Zhang, N. Zheng, Z. Xie and Y. Liu, *ACS Energy Lett.*, 2021, **6**, 1521.
20 H. Opoku, J. H. Lee, J.-J. Lee, H. Ahn and J. W. Jo, *ACS Mater. Lett.*, 2022, **4**, 2515.
21 Y. Bai, Z. Zhou, Q. Xue, C. Liu, N. Li, H. Tang, J. Zhang, X. Xia, J. Zhang, X. Lu, C. J. Brabec and F. Huang, *Adv. Mater.*, 2022, **34**, 2110587.
22 H.-S. Lin, T. Doba, W. Sato, Y. Matsuo, R. Shang and E. Nakamura, *Angew. Chem., Int. Ed.*, 2022, **61**, e202203949.
23 Q. Fu, H. Liu, S. Li, T. Zhou, M. Chen, Y. Yang, J. Wang, R. Wang, Y. Chen and Y. Liu, *Angew. Chem., Int. Ed.*, 2022, **61**, e202210356.
24 Q. Fu, X. Tang, H. Liu, R. Wang, T. Liu, Z. Wu, H. Y. Woo, T. Zhou, X. Wan, Y. Chen and Y. Liu, *J. Am. Chem. Soc.*, 2022, **144**, 9500.
25 X. Wang, Z. He, H. Chen, L. Yao, C. Li, X. Lin, Z. Zhou, K. Li, W. Wang, W. Cai, Q. Ling and H. Zhen, *Adv. Funct. Mater.*, 2023, **33**, 2308435.
26 S.-K. Kim, J. Kim, S. Choi, T. Yong, J. Y. Park, G. Lee, S. Han, H. R. You, S. Ko, G. Park, H. Ahn, J. Yang, Y. Kim, B. J. Kim and J. Choi, *Adv. Energy Mater.*, 2023, **13**, 2301927.
27 Y. Cai, Y. Zhang, J. Zhang, X. Pan, M. R. Andersson and P. Wang, *Angew. Chem., Int. Ed.*, 2024, **63**, e202315814.
28 J. J. H. McDowell, *Acta Crystallogr., Sect. B: Struct. Crystallogr. Cryst. Chem.*, 1976, **32**, 5.
29 J.-M. Raimundo, P. Blanchard, P. Frère, N. Mercier, I. Ledoux-Rak, R. Hierle and J. Roncali, *Tetrahedron Lett.*, 2001, **42**, 1507.
30 A. K. Mohanakrishan, P. Amaladass and J. A. Clement, *Tetrahedron Lett.*, 2007, **48**, 539.
31 P. Amaladas, J. A. Clement and A. K. Mohanakrishan, *Tetrahedron*, 2007, **63**, 10363.
32 K. Yamazaki, J. Kuwabara and T. Kanbara, *Macromol. Rapid Commun.*, 2013, **34**, 69.

33 S. J. Choi, J. Kuwabara and T. Kanbara, *ACS Sustainable Chem. Eng.*, 2013, **1**, 878.
34 F. Grenier, B. R. Aïch, Y.-Y. Lai, M. Guérette, A. B. Holmes, Y. Tao, W. W. H. Wong and M. Leclerc, *Chem. Mater.*, 2015, **27**, 2137.
35 S. Narayanan, S. P. Raghunathan, S. Mathew, M. V. M. Kumar, A. Abbas, K. Sreekumar, C. S. Kartha and R. Joseph, *Eur. Polym. J.*, 2015, **64**, 157.
36 W. Li and T. Michinobu, *Polym. Chem.*, 2016, **7**, 3165.
37 Y. Kojima, S. Hayashi and T. Koizumi, *J. Polym. Sci., Part A: Polym. Chem.*, 2017, **55**, 1183.
38 Y. Zhang, Y. Ren, X. Xie, Y. Wei, L. He, L. Fang, J. Zhang, Y. Yuan and P. Wang, *Adv. Funct. Mater.*, 2022, **32**, 2108855.
39 Z.-R. Tan, Y.-Q. Xing, J.-Z. Cheng, G. Zhang, Z.-Q. Shen, Y.-J. Zhang, G. Liao, L. Chen and S.-Y. Liu, *Chem. Sci.*, 2022, **13**, 1725.
40 Y. Zhang, L. He, Y. Cai, J. Zhang and P. Wang, *Angew. Chem., Int. Ed.*, 2024, **63**, e202401605.
41 Y.-J. Cheng, S.-Y. Yu, S.-C. Lin, J. T. Lin, L.-Y. Chen, D.-S. Hsiu, Y. S. Wen, M. M. Lee and S.-S. Sun, *J. Mater. Chem. C*, 2016, **4**, 9499.
42 M. Wakioka, H. Morita, N. Ichihara, M. Saito, I. Osaka and F. Ozawa, *Macromolecules*, 2020, **53**, 158.
43 H. Saito, J. Chen, J. Kuwabara, T. Yasuda and T. Kanbara, *Polym. Chem.*, 2017, **8**, 3006.
44 Z. Qian, Z. Cao, L. Galuska, S. Zhang, J. Xu and X. Gu, *Macromol. Chem. Phys.*, 2019, **220**, 1900062.
45 H. Bässler and A. Köhler, *Top. Curr. Chem.*, 2012, **312**, 1.
46 T. W. Barrett, H. Wohltjen and A. Snow, *Nature*, 1983, **301**, 694.
47 D. M. de Leeuw, M. M. J. Simenon, A. R. Brown and R. E. F. Einerhand, *Synth. Met.*, 1997, **87**, 53.
48 C. G. Shuttle, R. Hamilton, J. Nelson, B. C. O'Regan and J. R. Durrant, *Adv. Funct. Mater.*, 2010, **20**, 698.
49 T. Li, Y. Zhang, M. Ren, Y. Mu, J. Zhang, Y. Yuan, M. Zhang and P. Wang, *Angew. Chem., Int. Ed.*, 2024, **63**, e202401604.
50 B. Yurash, D. X. Cao, V. V. Brus, D. Leifert, M. Wang, A. Dixon, M. Seifrid, A. E. Mansour, D. Lungwitz, T. Liu, P. J. Santiago, K. R. Graham, N. Koch, G. C. Bazan and T.-Q. Nguyen, *Nat. Mater.*, 2019, **18**, 1327.
51 H. Makki, C. A. Burke and A. Troisi, *J. Phys. Chem. Lett.*, 2023, **14**, 8867.
52 M. Seifrid, G. N. M. Reddy, B. F. Chmelka and G. C. Bazan, *Nat. Rev. Mater.*, 2020, **5**, 910.
53 V. Coropceanu, J. Cornil, D. A. da Silva Filho, Y. Olivier, R. Silbey and J.-L. Brédas, *Chem. Rev.*, 2007, **107**, 926.
54 S. Olthof, S. Mehraeen, S. K. Mohapatra, S. Barlow, V. Coropceanu, J.-L. Brédas, S. R. Marder and A. Kahn, *Phys. Rev. Lett.*, 2012, **109**, 176601.
55 M. Schwarze, C. Gaul, R. Scholz, F. Bussolotti, A. Hofacker, K. S. Schellhammer, B. Nell, B. D. Naab, Z. Bao, D. Spoltore, K. Vandewal, J. Widmer, S. Kera, N. Ueno, F. Ortmann and K. Leo, *Nat. Mater.*, 2019, **18**, 242.
56 F. Li, X. Deng, F. Qi, Z. Li, D. Liu, D. Shen, M. Qin, S. Wu, F. Lin, S.-H. Jang, J. Zhang, X. Lu, D. Lei, C.-S. Lee, Z. Zhu and A. K.-Y. Jen, *J. Am. Chem. Soc.*, 2020, **142**, 20134.
57 G. A. H. Wetzelaer, M. Kuik, M. Lenes and P. W. M. Blom, *Appl. Phys. Lett.*, 2011, **99**, 153506.
58 J. Bisquert and I. Mora-Seró, *J. Phys. Chem. Lett.*, 2010, **1**, 450.
59 S. Yoo, B. Domercq and B. Kippelen, *J. Appl. Phys.*, 2005, **97**, 103706.
60 Y. Ren, M. Ren, X. Xie, J. Wang, Y. Cai, Y. Yuan, J. Zhang and P. Wang, *Nano Energy*, 2021, **81**, 105655.
61 X. Lin, G. E. Purdum, Y. Zhang, S. Barlow, S. R. Marder, Y.-L. Loo and A. Kahn, *Chem. Mater.*, 2016, **28**, 2677.
62 A. Fediai, F. Symalla, P. Friederich and W. Wenzel, *Nat. Commun.*, 2019, **10**, 4547.
63 Y. Yuan and J. Huang, *Acc. Chem. Res.*, 2016, **49**, 286.